Formation of highly doped nanostripes in 2D transition metal dichalcogenides via dislocation climb mechanism

Yung-Chang Lin[1]*, Jeyakumar Karthikeyan[2,3], Yao-Pang Chang[4], Shisheng Li[5], Silvan Kretschmer[6], Hannu-Pekka Komsa[2,7], Po-Wen Chiu[4], Arkady V. Krasheninnikov[6,2]*, Kazu Suenaga[1]*

[1]National Institute of Advanced Industrial Science and Technology (AIST), Tsukuba 305-8565, Japan

[2]Department of Applied Physics, Aalto University, P.O. Box 11100, 00076 Aalto, Finland

[3]Department of Basic Sciences and Humanities, Rajiv Gandhi Institute of Petroleum Technology, Jais, Amethi-229304, Uttar Pradesh, India

[4]Department of Electrical Engineering, National Tsing Hua University, Hsinchu 30013, Taiwan

[5]International Center for Young Scientists (ICYS), National Institute for Materials Science (NIMS), Tsukuba 305-0044, Japan

[6]Institute of Ion Beam Physics and Materials Research, Helmholtz-Zentrum Dresden-Rossendorf, 01328 Dresden, Germany

[7]Microelectronics Research Unit, University of Oulu, P.O. Box 8000, 90014 Oulu, Finland

Abstract

Doping of materials beyond the dopant solubility limit remains a challenge, especially when spatially non-uniform doping is required. In two-dimensional materials with a high surface-to-volume ratio, such as transition metal dichalcogenides, various post-synthesis approaches to doping have been demonstrated, but full control over spatial distribution of dopants remains a challenge. We performed a post-growth doping of single layers of WSe_2 by adding transition metal (TM) atoms in a two-step process, which includes annealing followed by deposition of dopants together with Se or S. The Ti, V, Cr, and Fe impurities at W sites were identified by using transmission electron microscopy and electron energy loss spectroscopy. Remarkably, an extremely high density (6.4%~15%) of various types of impurity atoms was achieved. The dopants revealed to be largely confined within nanostripes embedded in otherwise pristine WSe_2. Our density functional theory calculations show that the dislocations assist the incorporation of dopant during

their climb and give rise to stripe of TM dopant atoms. This work demonstrates a possible spatially controllable doping strategy to achieve the desired local electronic, magnetic, and optical properties in 2D materials.

Keywords: Doping, transition metal dichalcogenide, dislocation migration, nanostripe, STEM

E-mail: yc-lin@aist.go.jp, a.krasheninnikov@hzdr.de, suenaga-kazu@aist.go.jp

Intentional doping of materials is an essential approach to modify their properties, which has been widely used to produce electronic and optical semiconductor devices with the desired characteristics. Doping of bulk and low-dimensional materials is normally implemented during the growth. However, there is a fundamental limitation on the maximum concentration of dopants defined by the solubility of the doping elements in the host material. Another problem with doping during the growth is the lack of control over spatial distribution of the dopants. To go beyond the solubility limit, post-growth processes such as ion implantation can be used, but this approach tends to create undesirable defects, whose removal then requires additional annealing steps.

Recently, lots of research attention has been focused on two-dimensional (2D) materials,[1,2] as they not only exhibit great variety in electronic characteristics ranging from insulators to metals, but also possess unique properties related to their reduced dimensionality. While 2D materials can be doped with the same methods as bulk systems, there are approaches that are unique to them. Due to the surface-only geometry, the doping in 2D materials can also be attained by: (1) physical/chemical adsorption, (2) ionic-liquid-gating, and (3) direct atomic substitution.[3,4]. The surface adsorption and

ionic-liquid-gating are basically equivalent to the implementation of charge transfer between the environment and the 2D materials, which are both very effective due the high surface to volume ratio of the 2D materials. However, the difficulties in integration of the system limit the practical applications of these approaches. The direct atomic substitution in 2D materials can be done via, e.g., sulfurization/selenization.[5] Alternatively, vacancies can be produced by irradiation[6,7] or thermal evaporation during annealing,[8] followed by the deposition of doping species. Direct substitution can also be achieved via ion implantation, but is technically difficult as it requires very low ion energies (below 100 eV) or needs an additional coating of buffer layer and post-annealing,[9] as otherwise the ions would pass through the atomically-thin target.[10,11] As for 2D transition metal dichalcogenides (TMDCs), the majority of the direct doping methods lead to doping in the chalcogen sublattice,[5] while controllable doping of these materials in the TM sublattice is extremely important, because the variation of their valence *d*-electrons occupancy results in extensive modification of their electronic structure, exciton characteristics,[12] magnetism,[13–15] and catalytic behavior.[16] Finally, as with bulk system, while the substitutional doping can be realized during growth by using chemical vapor transport (CVT) or chemical vapor deposition (CVD) techniques,[17] the control over the spatial distribution of dopants still remains challenging, and doping concentrations less than 7 % are normally achievable.[18–24] Thus, a spatially controlled post-growth method for doping in the TM sublattice is still missing.

Here, we demonstrate a two-step method including post-annealing and doping to introduce TM dopants with a high concentration and spatial localization into 2D WSe_2. The dopants are found to be entirely confined within nanostripe regions with widths of about 3 nm. Sulfurization performed together with doping is used to reveal the doping

mechanism. The creation of chalcogen deficiency and formation of dislocations are the necessary ingredients to assist in the foreign TM substitution. While the dislocation core migrates along either zigzag or armchair directions, the substitutional TM dopants are concurrently embedded in the formed nanostripe. This is fundamentally different from the other above-mentioned doping methods, since the atoms are not replaced directly, but rather new material is added in the paths traversed by the climbing dislocation.

Single-layer WSe_2 flakes were first grown on sapphire by using chemical vapor deposition (CVD). Then, selenium vacancies were created due to sublimation of Se atoms at the upper atomic plane during the annealing at 740°C for 20 min with hydrogen flow. Afterwards, the Se vapor and Fe_2O_3 dopants were supplied again in the 2^{nd} step. The Fe doped WSe_2 sheets were transferred to quantifoil TEM grid for scanning transmission electron microscopy (STEM) observation. Figure 1a shows an annular dark field (ADF) image of the Fe doped WSe_2, where Fe dopants are not distributed homogeneously, but are concentrated along certain lines highlighted by green ribbons. The dopants are locally distributed either along the zigzag (orange dashed line) or armchair (white dashed line) directions as shown in the magnified ADF image in Figure 1b. On larger scale, we have found the doping lines are mainly parallel to the armchair direction of the WSe_2 lattice as shown in the Figure S1.

The linearly distributed dopants made us infer that this doping strategy may lead to more universal choice of dopant elements. In order to get more insight into the origin of the spatially localized distribution of dopants and to validate the hypothesis of multiple element doping, we selected four distinct metal oxides (Cr_2O_3, Fe_2O_3, MoO_3, Ta_2O_5) used for the doping source together with S vapor instead of Se in the 2^{nd} growth step. Details

of the growth and doping protocols can be found in Figure S2. Figure 1c shows an ADF image of the sulfurized WSe_2 specimen. The WSe_2 was transformed into lamellar phase consisting of WSeS Janus[25,26] domains with WS_2 nanostripes after the sulfurization. Here the orange arrows indicate the possible growth direction of the WS_2 nanostripes. The existence of WSeS Janus and WS_2 nanostripes can be distinguished directly from the ADF contrast, since the contrast is proportional to the atomic number (W(79), Se(32), S(16)), and heavier atoms give rise to brighter contrast.[27,28] Figure S3 shows the comparison of ADF intensity profile of WS_2 nanostripe and WSeS domain, as well as the Raman and PL analyses. Our Raman and PL survey shows that the WS_2 nanosritpes and WSeS domains are distributed quite uniformly over the whole specimen. One can see the existence of WSeS and WS_2 domains in the sulfurized WSe_2 specimen according to the Ramand and PL spectra. Chemical analysis was also performed on the WS_2 nanostripe and WSeS domains by using the electron energy loss spectroscopy (EELS). The corresponding EEL spectra are shown in the inset of Figure 1c. Importantly, high density of dopants was confined within the WS_2 nanostripes, which appeared in a darker ADF contrast as selectively marked by yellow circles, and none of them was found in the WSeS domains. A wider WS_2 domain can also be formed by aligning multiple WS_2 nanostripes next to each other. This gives rise to a fundamental question: how do the nanostripe structures form and why is dopant substitution found only within the nanostripes?

We studied the terminal part of the WS_2 nanostripe as shown in the ADF image in Figure 1d. The corresponding strain field contour performed by geometric phase analysis (GPA) is shown in Figure 1e, where two point-defects were detected and marked by red-dotted circles. These two point-defects (red dotted circle 1 and 2) correspond to dislocation cores (5-7 defects) as shown in Figure 1f and 1g, respectively. Similarly, the

WS_2 nanostripe structures were observed in the sulfurized $MoSe_2$ specimens,[5] and the dislocation cores can be found at the tip of the sulfurized domain. To get further insight into the role of strain and to highlight local strain concentration, we carried out geometric phase analysis (GPA), which is based on calculations of the structural deformation by comparing the structure with the reference crystalline area. Any topological defect such as the dislocation core will be easily detected due to the prominent compressive and tensile strains, while the substitutional point defects will hardly show up in the strain maps. The large amount of point defects in Figure 1d are all substitutional dopants which do not provide significant structure deformation. The existence of dislocation cores at the tip of the WS_2 nanostripes suggest that the formation of nanostriped doped areas is related to the presence of dislocations, and specifically, their cores.

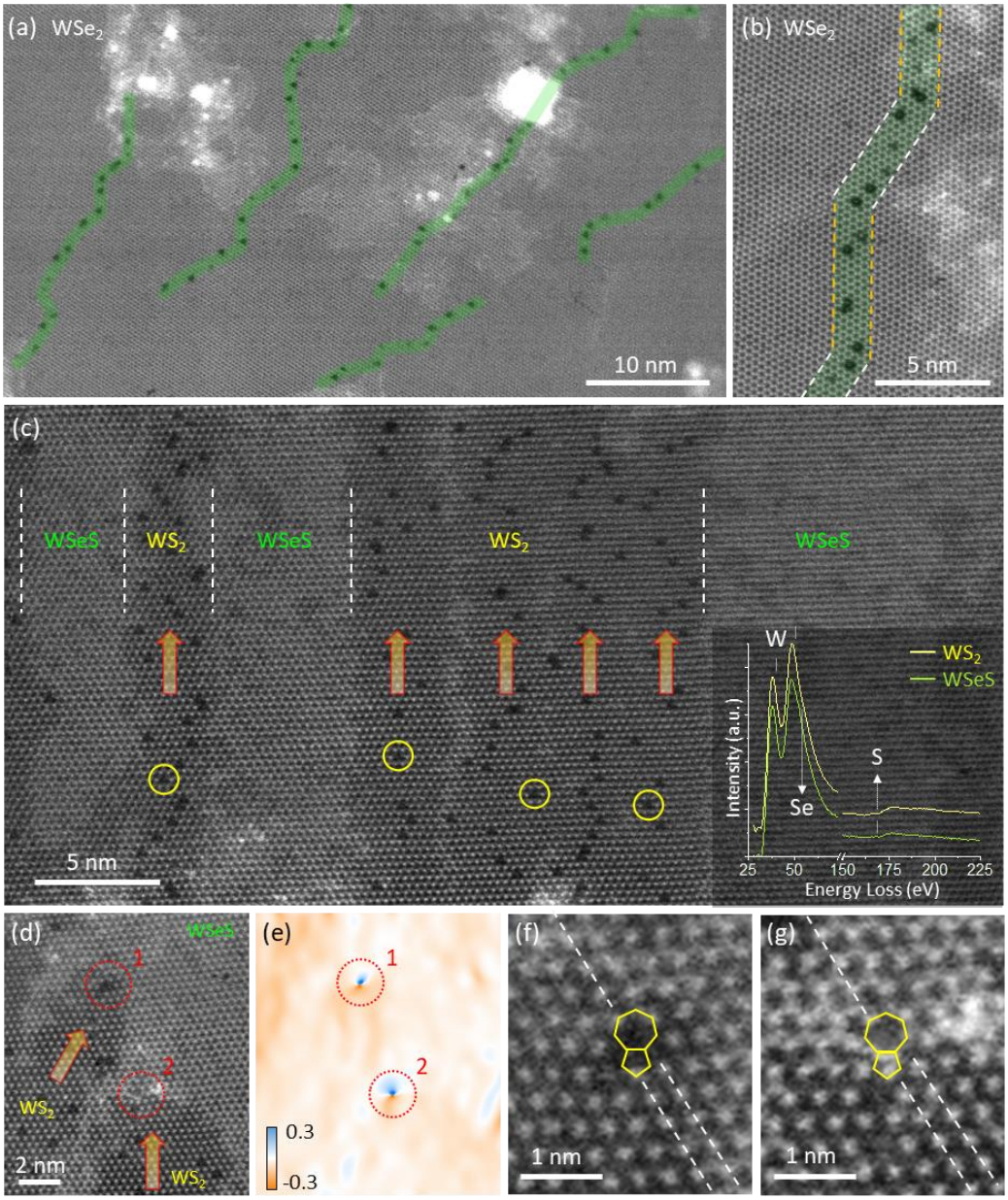

Figure 1. (a) Low magnification ADF image of Fe doped WSe_2. The Fe dopants are distributed in a linear trend highlighted by green stripes. (b) Magnified ADF image of Fe doped WSe_2. The Fe dopants exist along the armchair (white dashed line) and zigzag (orange dashed line) direction. (c) ADF image of parallel WS_2 nanostripes embedded in WSeS layer. Yellow circles selectively indicate the substitutional TM dopants. The inset shows the EELS spectra from the WS_2 nanostripe and WSeS layer. (d) ADF image of two terminating edges of WS_2 nanostripes. (e) The corresponding strain mapping of ε_{xx}

contour of (d) by GPA analysis. Red circles indicate the location of dislocation cores in (d). (f,g) Magnified ADF image of the 5-7 defects from the red circles 1 and 2 in (d), respectively. White dashed lines show the misaligned lattice at the point defects.

We performed chemical analyses for atom-by-atom identification of the dopant elements at each dopant sites. Figure 2a shows an ADF image of a WS_2 nanostripe with a size of 26.5 nm^2 consisting of 10 substitutional dopants. The colored circles represent the different metal dopants identified by EELS, and the corresponding EELS spectra are shown in Figure 2b. We found these dopants are TM elements, Ti, V, Cr, and Fe, substituting for W atoms. The Ti and V dopants are unintentional impurities probably originating from the Fe_2O_3 or Ta_2O_5 source materials. It is worth noting that the dopants can take positions in the lattice next to each other to form closest packed tri-dopants. The green dotted circle in Figure 2a highlights the defect consisting of Ti, Cr, and Fe atoms. As we know from previous studies, such defect configurations give rise to different defect-induced gap states as compared to those due to single defects.[12,22] The three TM atoms can also be directly distinguished by the ADF contrast as the difference in the atomic numbers, Ti(22), Cr(24), and Fe(26). In addition, we found that the three-element defect can consist of various distinct compositions as shown in the yellow dotted triangles in Figure 2c. The combinations of three TM elements in triangles are very different from one to another. Figure 2d-2h show the magnified ADF images of the tri-dopants marked by yellow triangles 1-5 in Figure 2c. One can distinguish the diversity of dopants directly from the ADF contrast, where the substituting elements are more and more heavy sequentially from Figure 2d to 2h (e.g., Cr, Fe, Nb, Mo, Ru). Two closest dopant

structures were also found as marked by blue trapezoids. The doping concentration in the WS_2 nanostripe is extremely high: 6.7% in average (counted from the white dotted square in Figure 2c), and it can be up to ~15% in some local areas (for example, the purple dashed square). Because the dopants are inhomogeneously distributed, the estimation of the doping concentration in the WS_2 nanostripe can vary a lot depending on the counting regions. Here we count the doping concentration by taking the whole WS_2 nanostrip in Figure 2c into account. There are 93 dopants substitute to the W sites, and the total number of W site in the WS_2 nanostripe is about 1,450, as shown in Figure S4. The doping concentration calculated from the whole WS_2 nanostripe in Figure 2c is about 6.4%. Based on our EELS statistics, the Cr and Fe are the most frequently found dopants among TMs, from the 4^{th} row of the Periodic Table, which represented about 60% of the total dopants. On the other hand, the number of Mo dopants (deduced from the ADF intensity) accounted for approximately 30% of the total dopants. The number of Ta dopant is difficult to measure in ADF, since its atomic number is only one unit smaller than W. No significant element-specific differences in the doping efficiencies are found. The concentration for distinct TM dopants should be mostly affected by the formation energy of TM dopant substitution. The vapor pressure of the doping source would be another factor to adjust the doing concentration. It would be ideal to use separate heating zones for distinct doping precursors to reach the highest doping level in future experiments.

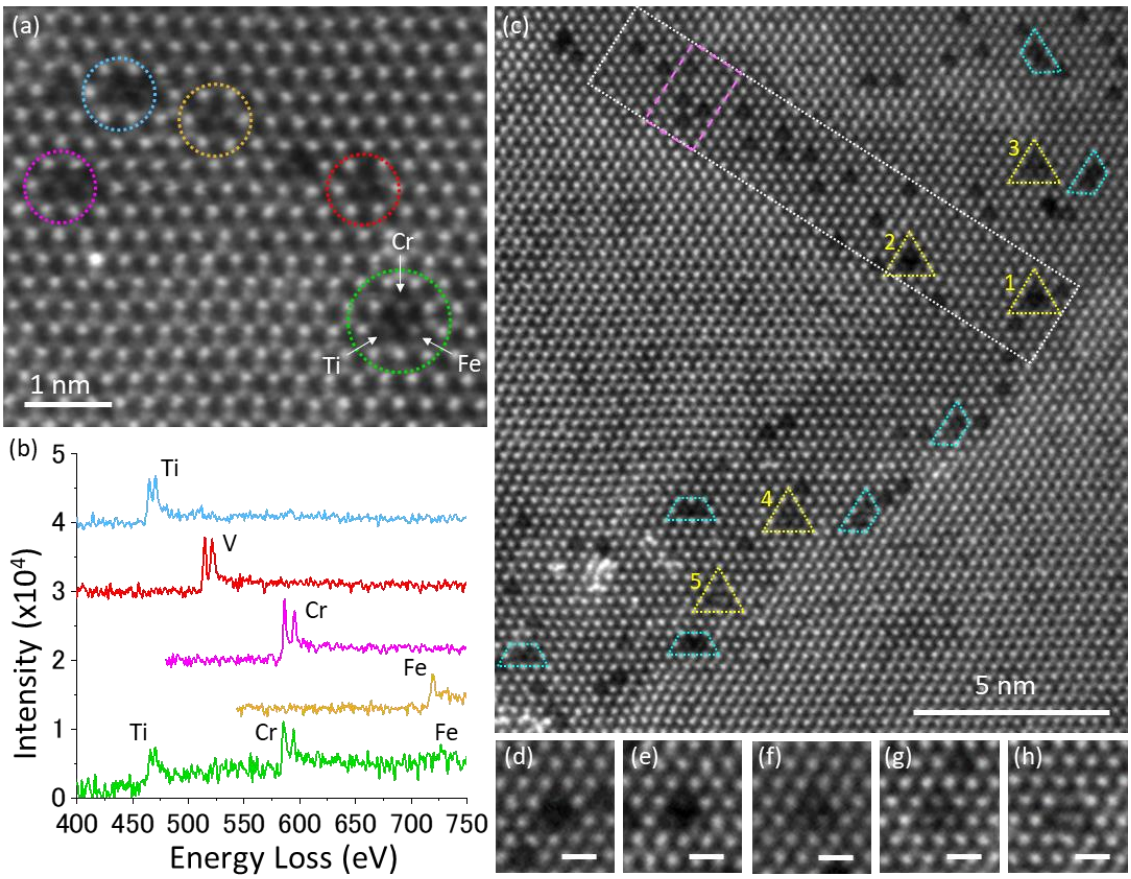

Figure 2. (a) ADF image of a WS_2 nanostripe in WSeS layer. Substitutional TM dopants are marked by color dotted circles. Cr, Fe and Ti forms three elements defect cluster marked by green dotted circle. (b) EELS spectra taken from the corresponding colored circles in (a). (c) ADF image of WS_2 nanostripe consisting of high density of TM atoms in WSeS layer. (d-h) Magnified ADF image corresponding to the dotted triangles 1-5 in (c). Scale bars are 0.5 nm.

As mentioned above, the growth of nanostripes with dopants is related to the presence of dislocation cores. The dislocations with the cores consisting of 5-7 rings are likely generated during the annealing process with Ar/H_2 flow. The surface Se atomic plane was

sublimated and a large number of Se as well as W vacancies were produced (Figure 3a), which cause structure reconstruction and formation of dislocations with 5-7 defects at their ends (Figure 3b). We stress that in a 2D system a finite-length dislocation is obviously a pair of point defects corresponding to its cores (one core, if the dislocation extends until the crystal edge). The dislocation can climb along the zigzag directions as pointed by red and blue arrows in Figure 3b. The dislocations eventually migrate along the armchair direction under a strain field, which is consistent with the previous studies without dopants[29,30]. Figure 3e schematically shows the mechanism of how the 5-7 dislocation core climbs in the WSe_2 lattice upon adsorption of metal and chalcogen atoms (light gray and light green balls located at the pink 5-7 defect). The metal and chalcogen atoms form bonds to the neighboring atoms and results in the climb of 5-7 defect toward the red or blue direction. In the case of selenization in the 2nd growth step, the Se gas flow carries the excess metal atoms to land on the specimen to fill the surface Se vacant sites. Then the WSe_2 nanostripes begin to grow from the dislocation cores when the Se supply is abundant and the foreign metal atoms can diffuse into the nanostripes during the 2nd growth step (Figure 3c and 3d). In the case of sulfurization, the S gas flow carries the excess metal atoms to fill in the surface Se vacant sites and form WSeS structure. Then the TM doped WS_2 nanostripes begin to grow from the dislocation cores when the S supply is abundant during the 2nd growth step. Note that a dislocation core remains at the end of the nanostripe.

On the other hand, the annealing can also create a line of W/Se vacancies (Figure 3f) and result in a dislocation of a finite length with a pair of cores as shown in Figure 3g. The dislocation cores can climb and migrate toward each other due to the driving force to fill these vacancy lines. Similarly, the chalcogen and metal dopants filled in to the

dislocation migration path during the 2nd step growth step (Figure 3h). Finally, the two dislocations annihilate and give rise to a WSe_2 or WS_2 nanostripe with dopants embedded in the original WSe_2 lattice coherently without a dislocation (Figure 3i). The situation of selenization and sulfurization is different, but the strain remains even when the vacancies are filled with S, thus leading to larger density of dislocations and thereby larger density of dopants, as can be seen by comparing Figures 1a and 1c. As is evident from the sketches shown in Figure 3, each row of atoms perpendicular to the nanostripe growth direction contains only one additional metal atom and, consequently, each row may contain at most one dopant atom. On the other hand, the STEM images in Figure 1 and 2 show that fairly large fraction of the rows indeed contain an impurity atom, and thus the doping efficiency is high.

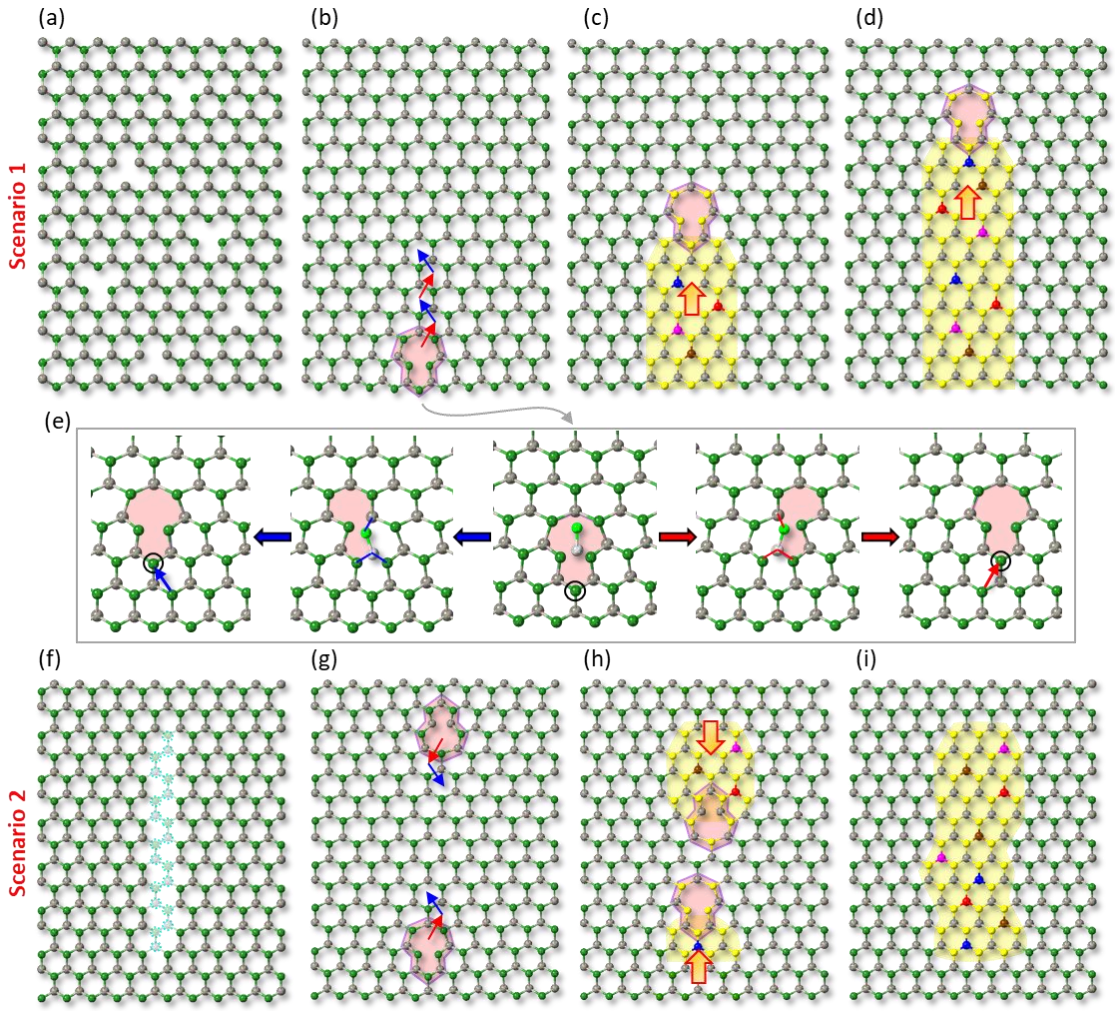

Figure 3. (a-d) Scenario 1: dislocation originates from the edge. (a) Schematic of defective WSe_2 during annealing. Se (green balls) and W (gray balls) defects are created at high temperature. (b) A dislocation core (5-7 defect) is created at the edge of WSe_2. The dislocation core can climb along the zigzag direction pointed by red and blue arrows. (c) Growth of nanostrip during the 2nd growth step with supply of chalcogen (yellow balls) and metal dopants (red, blue, brown, and magenta balls). (d) The doped nanostripe with a dislocation at the tip. (e) Schematic of the dislocation core climbing with the supply of extra metal and chalcogen atoms. (f-i) Scenario 2: dislocation pair originates from a line of vacancies. (f) Schematic of WSe_2 with a line of W/Se vacancies (marked by cyan dotted

circles) is created during the annealing process. (g) The formation of a pair of dislocation cores after the structural reconstruction. (h) The two dislocation pairs migrate toward each other during the 2nd growth step with the supply of chalcogen and metal dopants. (i) Elimination of the dislocation pair and left the grown nanostripe with TM dopants.

In order to validate the scenario presented in Figure 3 and better understand the spatially non-uniform incorporation of TM atoms in the atomic network of TMDs, we performed density functional theory (DFT) calculations as detailed below. A dislocation line was created in a rectangular periodic supercell by removing 8 W and 16 Se atoms, as schematically illustrated in Figure 3f-3i and in Figure 4a, then the geometry of the system was optimized, which gave rise to the formation of new bonds, so that the "cut" disappeared leaving just two dislocation cores. This gave rise to the development of tensile strain in the system. In order to understand if it is energetically favorable for TM atoms to be incorporated as substitutional dopants into the atomic network in the strained area as compared to the pristine (unstrained) lattice, we calculated the energetics of the system for Ti, V, Cr and Fe atoms in the positions of W atoms, which are indicated in Figure 4a. Position labelled "1", which is outside the strained area, was taken as the reference. The results of geometry optimization indicate that TM atoms prefer to be close to the dislocation cores, that is in positions 4, 5 and 10. To get further insight into the actual mechanism of the formation of the stripes, we also studied the energetics of TM atoms in the positions of adatoms. We found that TM atoms on top of WSe_2 sheet can form stable/metastable configurations: in addition to obvious high-symmetry positions on top of W atom or on top of the hollow area, TM atoms can also take the position in the middle of the hollow area, but below Se atoms, as shown in the inset in Figure 4c. To

differentiate this configuration from substitutional position, we refer to this configuration also as “adatom”. We note that the quantities presented in Figure 4b,c are the differences in the formation energy of the impurity depending on its spatial location, not the formation energy (absolute value) of a defect configuration. It indicates how much energy is released when the impurity moves closer to the dislocation area. We found that it is energetically favorable for adatoms in all configurations to be in the strained area, especially on the line between the dislocation cores, where strain is maximal, which is in line with the previous observations of TM adatom migration and localization on strained graphene[31]. This can be explained using simple arguments: strain gives rise to bond elongation, which makes the bonds weaker and, in turn, provides more electron density for forming new bonds with the adsorbed species. The lowest energy configuration for all TM atoms is the position in the heptagon with paired Se atoms (next to position 9). The TM atom breaks the Se-Se bonds and takes a position within the W plane, as shown in the red frame in Figure 4a. Thus one can assume that the adsorbed TM atoms will first migrate into the strained area and then will be incorporated into the atomic network at the cores of the dislocations. Our calculations further show that adding S or Se atoms (as dimers) markedly lowers the total energy of the system by -3.84, -3.93, -4.21, and -3.26 eV for Ti, V, Cr, and Fe (with respect to the dimer adsorbed on the pristine surface) and explain the mechanism of the dislocation climb (Figure 3e) and eventual disappearance. To get a comprehensive picture, we also studied the energetics of TM atoms in other positions, e.g., in X-sub positions reported for Mo-based TMDs,[14] and also investigated in more detail the behavior of TM atoms in WS_2 and Janus WSeS system. The results are presented in Figure S5. The analysis of the obtained data indicates that the substitutional positions in W sites are always preferable, the presence of vacancies facilitates the

substitution, and that the behavior is qualitatively the same for all the systems, generalizing our findings.

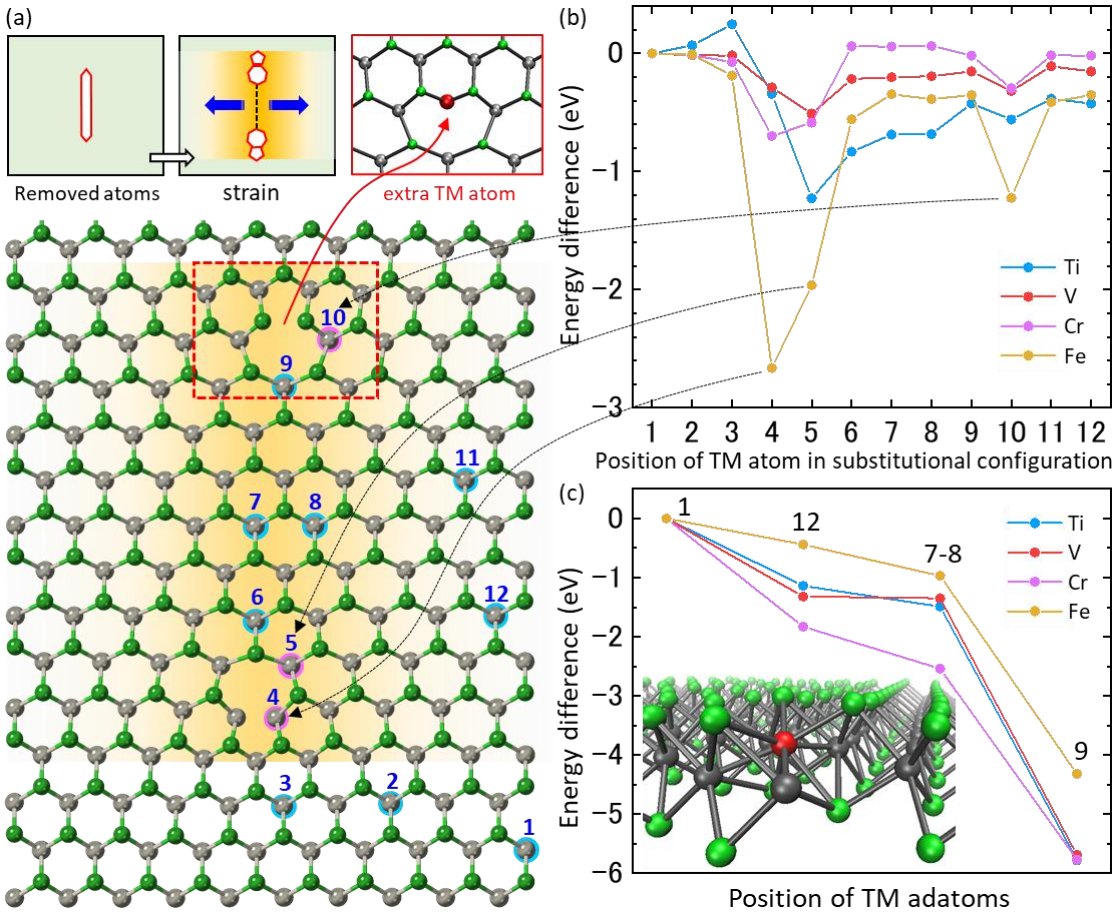

Figure 4. (a) Atomic model of WSe_2 sheet with a dislocation line created by removing W and Se atoms, as schematically illustrated in the inset, and the resulting strain distribution (orange shading). Green balls represent Se and grey stand for W atoms. (b) The energies of TM atom in substitutional (W) positions labelled in panel (a). The energy of the TM atom in position "1", which is outside the strained area, is taken as the reference (zero) energy. It is evident that TM atoms in the substitutional positions prefer to be in the strained areas next to the dislocation cores. (c) The relative energies of TM adatoms placed at various positions. The inset shows a configuration when the adatom (red ball)

takes the position the middle of the hollow area, but below Se atoms. Adatoms prefer to be in the strained area and ultimately take the position in the heptagon, with the atomic configuration being shown in panel (a) in the red frame.

In summary, we have demonstrated a novel doping strategy for TMDCs based on a dislocation climb mechanism in the presence of excess doping atoms. In a wider context, our findings provide a tool for tracing the dislocation migration path in 2D materials by its trail of dopants. We note that the proposed dislocation-mediated doping mechanism is heavily based on static first-principles calculations carried out at zero temperature, which do not exactly reproduce the experimental conditions. Thus, this is just a likely scenario, which may also be relevant to the doping of materials during their growth. In situ STEM imaging during the growth might give an experimental evidence in the future. The most important result is that the dopants are confined to the linear paths of the dislocation climb at high concentrations. Such kind of special 1D heterostructures embedded in 2D planes possess enormous flexibility and controllability to tailor the electronic structures and magnetic properties with high spatial resolution especially when vacancies are created in the pre-designed areas and possibly controlled by external strain. This technique can be greatly beneficial to the fabrication of electronic devices with specific purpose to realize 1D spin injection channels, spatially confined superconducting channels, light emitting gratings, high-entropy lamellar materials, or high efficiency electrocatalysts for fuel cells, metal-air batteries and electrolyzers.

Experimental:

Two step doping growth method

To proceed the post-growth substitutional doping of TM atoms, single-layer WSe_2 flakes were firstly grown on sapphire substrate using chemical vapor deposition (CVD). Post-growth substitutional doping of WSe_2 were carried out in a 3-inch home-made CVD furnace. Creation of chalcogen vacancies is essential for the substitution of tungsten atoms. Firstly, the grown WSe_2 samples were placed at the center of the furnace and annealed at 700°C for 20 min, during which massive Se atoms at the surface sublayer sublime with the aid of hydrogen at the elevated temperature. Secondly, TM dopants were also supplied for the dopant embedment in host lattice. The oxide powder was placed ca. 3 cm away from the WSe_2 samples at the upstream side of gas flow. Transition metal oxide was used as the source of dopants, e.g., Cr_2O_3 (Alfa Aesar 99%), Fe_2O_3 (Alfa Aesar 98%), MoO_3 (Sigma-Aldrich 99.5%), and Ta_2O_5 (Alfa Aesar 99%) for Cr, Fe, Mo, and Ta doping, respectively. The selenium or sulfur powder (~300 mg) was also placed at the upstream side of the gas flow, with temperature controlled by an independent induction heater at 160~170°C. Selenium or sulfur vapors were introduced to carry the TM atoms and to repair the lattice structure during the 2^{nd} doping growth process. Details of the growth and doping protocols can be found in the Supporting Information. It should be noted that using sulfur instead of selenium in the second CVD step is advantageous to label and trace the chemical reaction.

STEM and EELS

STEM images were acquired by using ARM200F based microscope equipped with a JEOL delta corrector and a cold field emission gun operating at 60 kV. The probe current

is about 20 pA. The convergence semi-angle and the inner acquisition semi-angle are is 37 mrad and 76 mrad. Typical ADF image was 1024 x 1024 pixels resolution captured by using 38.5 μs pixel time. The EELS core loss spectra were taken by using Gatan Rio CMOS camera optimized for low-voltage operation. EEL spectrum was acquired by using line scan with exposure time of 0.1 sec/pixel.

DFT calculation

Density-functional theory calculations were carried out using VASP software package.[32,33] We used the PBE exchange-correlation functional[34] and plane-wave cutoff of 500 eV. The possible spin-polarization was always accounted for. The dislocation line was created in a rectangular $10x8\sqrt{3}$ supercell consisting of 480 atoms by removing 8 W and 16 Se atoms. The Brillouin zone was samples with the sole Γ-point. Defects in pristine WS_2, WSe_2, and WSeS were modeled using 6x6 supercell and using k-point mesh of 3x3. The electronic relaxations were carried out with the convergence criteria of 10^{-6} and the forces on all the ions were relaxed below 0.01 eV/Å.

Acknowledgement

Y.-C.L. and K.S. acknowledge to the JSPS-KAKENHI (JP16H06333), (18K14119), JST-CREST program (JPMJCR20B1, JMJCR20B5, JPMJCR1993), JSPS A3 Foresight Program, and Kazato Research Encouragement Prize. H.-P.K. acknowledges funding from Academy of Finland through project no. 311058. AVK thanks the German Research Foundation (DFG), project KR 4866/2-1 for support. We thank CSC Finland, HRLS Stuttgart, Germany and TU Dresden (Taurus cluster) for the generous grants of computer time. P.-W.C. appreciates the project support of Taiwan Ministry of Science and

Technology: Grants MOST 107-2119-M-007-011-MY2 and MOST 106-2628-M-007-003-MY3. S.L. acknowledges the support from JSPS-KAKENHI (19K15399).

References

[1] M. Chhowalla, H. S. Shin, G. Eda, L.-J. Li, K. P. Loh, H. Zhang, *Nat. Chem.* **2013**, *5*, 263.

[2] F. Xia, H. Wang, D. Xiao, M. Dubey, A. Ramasubramaniam, *Nat. Photonics* **2014**, *8*, 899.

[3] P. Luo, F. Zhuge, Q. Zhang, Y. Chen, L. Lv, Y. Huang, H. Li, T. Zhai, *Nanoscale Horizons* **2019**, *4*, 26.

[4] K. Zhang, J. Robinson, *MRS Adv.* **2019**, *4*, 2743.

[5] S.-H. Su, W.-T. Hsu, C.-L. Hsu, C.-H. Chen, M.-H. Chiu, Y.-C. Lin, W.-H. Chang, K. Suenaga, J.-H. He, L.-J. Li, *Front. Energy Res.* **2014**, *2*, 1.

[6] Y. C. Lin, C. Y. Lin, P. W. Chiu, *Appl. Phys. Lett.* **2010**, *96*, DOI 10.1063/1.3368697.

[7] Y. C. Lin, P. Y. Teng, C. H. Yeh, M. Koshino, P. W. Chiu, K. Suenaga, *Nano Lett.* **2015**, *15*, 7408.

[8] R. J. Chang, Y. Sheng, G. H. Ryu, N. Mkhize, T. Chen, Y. Lu, J. Chen, J. K. Lee, H. Bhaskaran, J. H. Warner, *ACS Appl. Mater. Interfaces* **2019**, *11*, 24279.

[9] S. M. He, C. C. Huang, J. W. Liou, W. Y. Woon, C. Y. Su, *ACS Appl. Mater. Interfaces* **2019**, *11*, 47289.

[10] U. Bangert, W. Pierce, D. M. Kepaptsoglou, Q. Ramasse, R. Zan, M. H. Gass, J. A. Van Den Berg, C. B. Boothroyd, J. Amani, H. Hofsäss, *Nano Lett.* **2013**, *13*,

4902.

[11] M. Tripathi, A. Markevich, R. Böttger, S. Facsko, E. Besley, J. Kotakoski, T. Susi, *ACS Nano* **2018**, *12*, 4641.

[12] Y.-C. Lin, S. Li, H.-P. Komsa, L.-J. Chang, A. V Krasheninnikov, G. Eda, K. Suenaga, *Adv. Funct. Mater.* **2017**, *1704210*, 1.

[13] X. L. Fan, Y. R. An, W. J. Guo, *Nanoscale Res. Lett.* **2016**, *11*, DOI 10.1186/s11671-016-1376-y.

[14] J. Karthikeyan, H.-P. Komsa, M. Batzill, A. V. Krasheninnikov, *Nano Lett.* **2019**, *19*, 4581.

[15] S. S. Guan, S. S. Ke, F. F. Yu, H. X. Deng, Y. Guo, H. F. Lü, *Appl. Surf. Sci.* **2019**, *496*, 143692.

[16] G. Liu, A. W. Robertson, M. M.-J. Li, W. C. H. Kuo, M. T. Darby, M. H. Muhieddine, Y.-C. Lin, K. Suenaga, M. Stamatakis, J. H. Warner, S. C. E. Tsang, *Nat. Chem.* **2017**, *9*, 810.

[17] Y. C. Lin, D. O. Dumcenco, H. P. Komsa, Y. Niimi, A. V. Krasheninnikov, Y. S. Huang, K. Suenaga, *Adv. Mater.* **2014**, *26*, 2857.

[18] Z. S. Wu, A. Winter, L. Chen, Y. Sun, A. Turchanin, X. Feng, K. Müllen, *Adv. Mater.* **2012**, *24*, 5130.

[19] L. Zhao, M. Levendorf, S. Goncher, T. Schiros, L. Pálová, A. Zabet-Khosousi, K. T. Rim, C. Gutiérrez, D. Nordlund, C. Jaye, M. Hybertsen, D. Reichman, G. W. Flynn, J. Park, A. N. Pasupathy, *Nano Lett.* **2013**, *13*, 4659.

[20] J. Gao, Y. D. Kim, L. Liang, J. C. Idrobo, P. Chow, J. Tan, B. Li, L. Li, B. G. Sumpter, T. M. Lu, V. Meunier, J. Hone, N. Koratkar, *Adv. Mater.* **2016**, *28*, 9735.

[21] K. Zhang, S. Feng, J. Wang, A. Azcatl, N. Lu, R. Addou, N. Wang, C. Zhou, J.

Lerach, V. Bojan, M. J. Kim, L. Q. Chen, R. M. Wallace, M. Terrones, J. Zhu, J. A. Robinson, *Nano Lett.* **2015**, *15*, 6586.

[22] J. Zhou, J. Lin, H. Sims, C. Jiang, C. Cong, J. A. Brehm, Z. Zhang, L. Niu, Y. Chen, Y. Zhou, Y. Wang, F. Liu, C. Zhu, T. Yu, K. Suenaga, R. Mishra, S. T. Pantelides, Z. G. Zhu, W. Gao, Z. Liu, W. Zhou, *Adv. Mater.* **2020**, *1906536*, 1.

[23] A. W. Robertson, Y.-C. Lin, S. Wang, H. Sawada, C. S. Allen, Q. Chen, S. Lee, G.-D. Lee, J. Lee, S. Han, E. Yoon, A. I. Kirkland, H. Kim, K. Suenaga, J. H. Warner, *ACS Nano* **2016**, *10*, 10227.

[24] J. Zhou, J. Lin, X. Huang, Y. Zhou, Y. Chen, J. Xia, H. Wang, Y. Xie, H. Yu, J. Lei, D. Wu, F. Liu, Q. Fu, Q. Zeng, C.-H. Hsu, C. Yang, L. Lu, T. Yu, Z. Shen, H. Lin, B. I. Yakobson, Q. Liu, K. Suenaga, G. Liu, Z. Liu, *Nature* **2018**, *556*, 355.

[25] J. Zhang, S. Jia, I. Kholmanov, L. Dong, D. Er, W. Chen, H. Guo, Z. Jin, V. B. Shenoy, L. Shi, J. Lou, *ACS Nano* **2017**, *11*, 8192.

[26] A. Y. Lu, H. Zhu, J. Xiao, C. P. Chuu, Y. Han, M. H. Chiu, C. C. Cheng, C. W. Yang, K. H. Wei, Y. Yang, Y. Wang, D. Sokaras, D. Nordlund, P. Yang, D. A. Muller, M. Y. Chou, X. Zhang, L. J. Li, *Nat. Nanotechnol.* **2017**, *12*, 744.

[27] S. J. Pennycook, *Ultramicroscopy* **1989**, *30*, 58.

[28] O. L. Krivanek, M. F. Chisholm, V. Nicolosi, T. J. Pennycook, G. J. Corbin, N. Dellby, M. F. Murfitt, C. S. Own, Z. S. Szilagyi, M. P. Oxley, S. T. Pantelides, S. J. Pennycook, *Nature* **2010**, *464*, 571.

[29] Y. Han, M. Y. Li, G. S. Jung, M. A. Marsalis, Z. Qin, M. J. Buehler, L. J. Li, D. A. Muller, *Nat. Mater.* **2018**, *17*, 129.

[30] W. Zhou, Y. Y. Zhang, J. Chen, D. Li, J. Zhou, Z. Liu, M. F. Chisholm, S. T. Pantelides, K. P. Loh, *Sci. Adv.* **2018**, *4*, eaap9096.

[31] O. Cretu, A. V. Krasheninnikov, J. A. Rodríguez-Manzo, L. Sun, R. M. Nieminen, F. Banhart, *Phys. Rev. Lett.* **2010**, *105*, 1.

[32] G. Kresse, J. Furthmüller, *Comput. Mater. Sci.* **1996**, *6*, 15.

[33] G. Kresse, J. Furthmüller, *Phys. Rev. B* **1996**, *54*, 11169.

[34] J. P. Perdew, K. Burke, M. Ernzerhof, *Phys. Rev. Lett.* **1996**, *77*, 3865.